A High-Precision, Magnetically Levitated Positioning Stage

Toward contactless actuation for industrial manufacturing

By Robert Brydon Owen, Manfredi Maggiore*, and Jacob Apkarian

Published in: Control Systems Magazine, vol. 26, no. 3, 2006, pp. 82-95

1 Introduction

High accuracy positioning stages with multiple degrees-of-freedom, or *microsteppers*, are ubiquitous in industrial manufacturing. These devices are used in probing and inspection systems, in the assembly of disk drive heads, and in semiconductor manufacturing. In semiconductor manufacturing, microsteppers are employed to accurately move silicon wafers in the photolithography process. To guarantee both speed and precision, microsteppers are usually composed of a lower stage, which actuates large high-speed movements, and an upper stage, which delivers short high-precision movements using piezoelectric actuators [1]. One such device, shown in Figure 1, delivers motion by means of mechanical contacts. Friction in mechanical contacts releases microscopic dust particles that limit the accuracy of the photolithographic process, thus reducing production throughput in semiconductor manufacturing [2]. For this reason, there is increasing interest in the semiconductor industry to replace mechanical microsteppers by magnetically levitated devices. Magnetically levitated microsteppers are an attractive alternative in other applications since their parts are not subject to mechanical wear and hence do not require extensive maintenance.

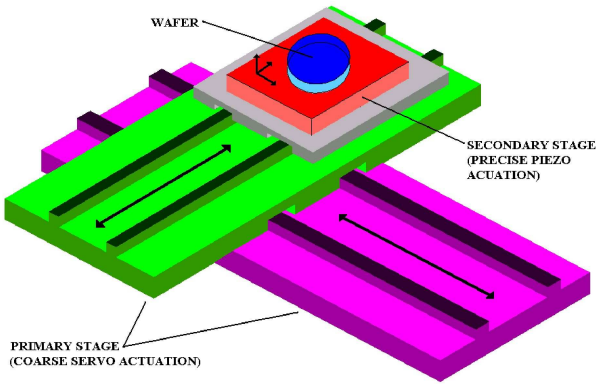

Figure 1: Structure of a conventional microstepper used in semiconductor manufacturing. The primary stage employs servomotors for fast and coarse 2DOF actuation. The secondary stage employs piezoelectric actuators for fine 3DOF or 6DOF regulation. The silicon wafer is placed on top of the secondary stage.

*Corresponding author. Address: Department of Electrical and Computer Engineering, University of Toronto, 10 King's College Road, Toronto, ON, M5S 3G4, CANADA. E-mail: maggiore@ control.utoronto.ca

In [3], a six-degree-of-freedom (DOF) device is designed using ten electromagnets placed within the interior of a cage structure that houses a movable platen. The planar range of motion of this device is 8×8 mm^2, while the air gap range is 4 mm. In [4], [5], [6], the authors develop magnetic levitation devices utilizing the principle of electromagnetic reluctance to achieve planar magnetic levitation with a range, in the latest prototype, of 130×130 mm^2. In [7],[8], a contactless microstepper employs air-cored permanent magnet linear synchronous motors (PMLSM) to actuate six DOFs. The planar range of motion of the device in [7] is 50×50 mm^2, while the air gap range is 400 μm. PMLSMs are ideally suited for building microsteppers. Since each PMLSM produces both normal and longitudinal forces, several PMLSMs can easily be assembled to control multiple DOFs yielding a device with a simple mechanical design. Moreover, PMLSMs allow for a large range of operation. In [9], an idealized 3DOF microstepper is investigated. Similarly to the microstepper developed in [7], the device in [9] employs PMLSMs as fundamental building blocks. The main difference with the device in [7] is that the PMLSMs in [9] are iron cored rather than air cored and the device in [9] uses standard permanent magnets rather than custom-design Halbach magnet arrays. This configuration is advantageous compared to previous implementations since iron-cored PMLSMs are commonly available on the market and require less current for levitation than their air-cored counterparts. The question remains, however, as to whether a physical implementation of an iron-cored PMLSM-based positioning system can be successfully implemented.

In this article we provide the experimental verification of the theoretical ideas found in [9]. This verification presents major challenges. First, the validity of the mathematical model of [9] must be assessed. Since unknown parameters enter the model, the model verification must rely on parameter identification. Next, a controller must be designed to achieve setpoint and sinusoidal tracking. Finally, the controller must decouple all DOFs.

Due to the difficulty of the experimental verification, we divide our research into two stages. We first implement a device that employs one PMLSM to actuate two DOFs (horizontal propulsion and vertical suspension) with range of operation 100 mm$\times$10 mm. Using this device, we assess the accuracy of the model of the forces found in [9]. A key ingredient is the parameter identification technique of [10]. We then design a nonlinear controller based on feedback linearization and output regulation for setpoint and sinusoidal tracking. We show experimentally that this controller yields superior performance to linearization-based output regulators.

Having tested the feasibility of a simple device, we develop an experimental setup that employs four PMLSMs to actuate three DOFs with a planar operating range of 100×100 mm^2, an air gap range of 10 mm, and a positioning accuracy of 10 μm. The experimental results show good performance for both setpoint and sinusoidal tracking over the entire operating range of the device.

2 PMLSM Operation

A permanent magnet linear synchronous motor (PMLSM) is composed of two parts, a *stator* and a *mover;* see Figure 2. The stator hosts a three-phase winding generating a magnetic field that travels along the linear axis. Depending on the stator core filling, a PMSLM is either air cored or iron cored. The mover is constructed of a series of permanent magnets of alternating polarity mounted on an iron backing.

In typical configurations, the axis normal to the linear motion is constrained at a fixed air gap by means of bearings, and the PMLSM is used to propel the mover along the linear axis. However, PMLSMs can generate both a longitudinal force along the linear axis and a normal force. These forces can be used for simultaneous propulsion and levitation. The longitudinal force is generated by the interaction between the magnetic charge of the permanent magnets and the traveling stator

field. For an iron-cored PMLSM, the normal force has two components:

(i) An attractive force between the permanent magnets of the mover and the iron core of the stator.

(ii) An attractive/repulsive force generated by the interaction between the permanent magnet fields and the field of the stator coils.

The permanent magnets in the mover can be designed so that component (i) of the normal force is slightly stronger than the gravity force when the mover is inside a predetermined operating range. The stator currents are regulated to generate a small repulsive normal force to achieve levitation. Thus, in iron-cored PMLSMs, small-amplitude stator currents are sufficient for levitation. In contrast, due to the absence of ferromagnetic material in the core of the motor, an air-cored PMLSM produces only component (ii) of the normal force. Thus, to achieve levitation, air-cored PMLSMs require larger stator currents than their iron-cored counterparts.

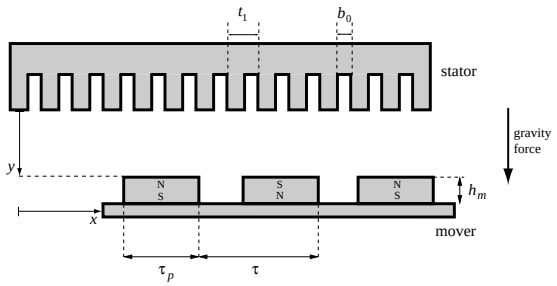

Figure 2: Structure of a flat, single-sided iron-cored PMLSM. A PMLSM is composed of two parts, a stator and a mover. The stator has slots hosting a three-phase winding. The mover, placed below the stator, hosts a series of permanent magnets of alternating polarity. The variables x and y denote the horizontal displacement of the mover relative to the stator and the air gap length, respectively.

3 Iron-Cored PMLSM Model

We next present a mathematical model of the longitudinal and normal forces, denoted F_x and F_y, generated by an iron-cored PMLSM. This model was developed in [9] based on [11],[12].
Referring to Figure 2, let x denote the horizontal displacement of the mover relative to the stator, and let y denote the air gap length. Define i_d and i_q as the direct and quadrature current inputs to the PMLSM. These inputs are related to the magnitudes I_a, I_b, and I_c of the phasors of the three-phase currents according to

$$\begin{bmatrix} i_d \\ i_q \end{bmatrix} = \frac{2}{3} \begin{bmatrix} \cos(\frac{\pi}{\tau}x) & \cos(\frac{\pi}{\tau}x - \frac{2\pi}{3}) & \cos(\frac{\pi}{\tau}x + \frac{2\pi}{3}) \\ -\sin(\frac{\pi}{\tau}x) & -\sin(\frac{\pi}{\tau}x - \frac{2\pi}{3}) & -\sin(\frac{\pi}{\tau}x + \frac{2\pi}{3}) \end{bmatrix} \begin{bmatrix} I_a \\ I_b \\ I_c \end{bmatrix}.$$

The longitudinal and normal forces on the mover are given by

$$F_x = -K_1(y) i_q, \tag{1}$$
$$F_y = -\left[K_2(y) + K_3(y) i_d + K_4(y)(i_d^2 + i_q^2)\right], \tag{2}$$

where

$$K_1(y) = \frac{12\sqrt{2} W k_{w1} p_m L_A \sigma_m \mu_0 \tilde{\lambda}(y) \sinh(\frac{\pi}{\tau} h_m) \sin(\frac{\pi \tau_p}{2\tau})}{\pi p K_c(y) \sinh(\frac{\pi}{\tau}(h_m + y))},$$

$$K_2(y) = \frac{\tilde{\lambda}(y) L_A p_m \tau B_{pmy1}(y)^2}{4\mu_0},$$

$$K_3(y) = -\frac{\tilde{\lambda}(y) 3\sqrt{2} L_A p_m W k_{w1} B_{pmy1}(y) \coth(\frac{\pi}{\tau}(h_m + y))}{p^2 K_c(y)},$$

$$K_4(y) = \frac{18 L_A p_m W^2 k_{w1}^2 \mu_0 \coth^2(\frac{\pi}{\tau}(h_m + y))}{\tau p^2 K_c(y)^2},$$

$$K_c(y) = \frac{t_1}{t_1 - y\gamma_1(y)},$$

$$\gamma_1(y) = \frac{4}{\pi}\left[\frac{b_0}{2y} \arctan\left(\frac{b_0}{2y}\right) - \ln\sqrt{1 + \left(\frac{b_0}{2y}\right)^2}\right],$$

$$k_{w1} = \frac{\sin\left(\frac{\pi}{6}\right)}{\frac{w_c}{3t_1}\sin\left(\frac{\pi t_1}{2\tau}\right)} \sin\left(\frac{\pi w_c}{2\tau}\right),$$

$$\tilde{\lambda}(y) = 1 - \frac{b_0^2}{4t_1(y + \frac{b_0}{2} + \frac{h_m}{\mu_{rec}})}.$$

The constant σ_m, denoting the magnetic surface charge density of the permanent magnets (see [11],[12] for a definition of magnetic surface charge density), is unknown and is not easily determined experimentally. The remaining constants in the above expressions characterize geometric and electromagnetic properties of a PMLSM. The description and numerical values of all constants are given in Table 1. The function $B_{pmy1}(y)$, which represents the magnetic field produced by the permanent magnets, is approximated using a 12^{th}-order polynomial.

4 2DOF Testbed

To verify the mathematical model of the longitudinal and normal forces in (1) and (2), we use a 2DOF positioning stage. This stage, designed and built by Quanser Consulting, employs one PMLSM to control the horizontal displacement x and the air gap length y; see Figure 3. The horizontal and vertical ranges of motion are 100 mm and 10 mm, respectively. The individual components of the system are described below.

The *stator* of the PMLSM, which is fixed in place to a heavy aluminum frame, is longitudinally laminated and transversally slotted to accommodate a single-layer three-phase winding. The *mover*, which is attached to a movable platform, is composed of four type-N35 permanent magnets attached to a ferromagnetic backing.

The mover of the PMLSM is mounted on a movable platform that constrains the motion to lie in a vertical plane. As shown in Figure 4, the platform slides on two horizontal linear guides, which are in turn supported by a base that slides vertically on four linear guides; see Figure 5. Using linear guides in this experiment has several benefits. First, the guides allow us to focus on the two DOFs

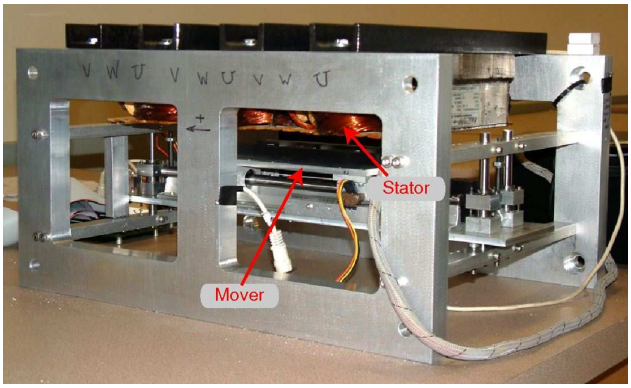

Figure 3: 2DOF magnetic levitation positioning stage. The stage employs one PMLSM to control the horizontal displacement x and the air gap length y. The stator of the motor is fixed in place to a heavy aluminum frame. The mover is a attached to a movable platen, which hosts four permanent magnets. The horizontal range of motion is approximately 100 mm, while the vertical displacement is approximately 10 mm.

we want to control by preventing the platform from pitching, rolling, and translating in an undesired direction. Furthermore, linear guides make it easy to include vertical and horizontal stoppers for adjusting the operating range of the platform and fixing either the horizontal or vertical motion of the system. Finally, linear guides facilitate incorporation of sensors. We employ two linear optical encoders with a resolution of 10 μm to measure the horizontal and vertical position of the platform. The velocities of the platform are estimated using high-gain observers. Since the linear guides introduce friction in the system, we plan to eliminate them in future generations of the experiment by employing multiple linear motors to control six DOFs.

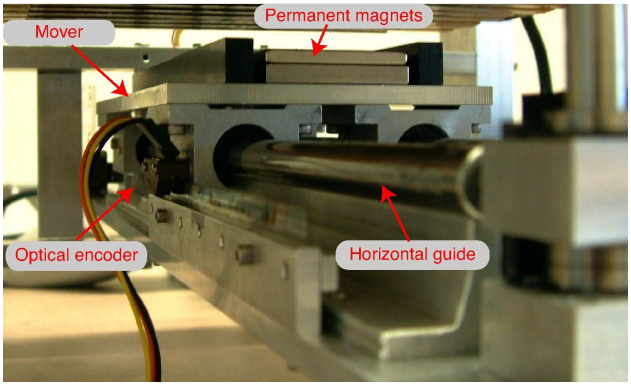

Figure 4: Closeup of horizontal linear guides. The linear guides secure the mover to the platform and allow for horizontal motion. The optical encoder measures the horizontal displacement of the mover with an accuracy of 10 μm.

The three-phase ac current required to actuate the stator coils is provided by three linear current amplifier modules (LCAMs) supplied by Quanser Consulting. Current commands are sent to the LCAMs through an interface from a PC. Each LCAM can supply 7 A continuous and 9 A peak. The power delivery is factory tuned to account for the inductance of the stator coils in the system. The positioning stage is connected to a standard PC running Windows XP using a Quanser Consulting Q8 board. The Q8 board, which provides all the necessary analog and digital I/O, is

Table 1: Specifications for the 2DOF positioning hardware. Many of the measurement values conform to industry standards. The mass M_h displaced horizontally and the mass M_v displaced vertically are different since the platform is constructed from separate components that move independently across each range of motion.

Parameter	Symbol	units	value
Stator slot width	b_0	mm	12.7
Stator slot pitch	t_1	mm	19.05
Turns per phase	W	–	900
Coil pitch	ω_c	mm	57.15
Stator pole pairs	p	–	3
Number of stator slots	z_1	–	18
Permanent magnet height	h_m	mm	5.0
Permanent magnet length	L_A	mm	50
Number of permanent magnets	p_m	–	4
Magnetic surface charge density of permanent magnets	σ_m	A/m	–
Pole pitch	τ	mm	57.15
Permanent magnet width	τ_p	mm	28.58
Permanent magnet coercivity	H_c	A/m	875400
Perm. magnet relative recoil permeability	μ_{rec}	–	1.1
Free space permeability	μ_0	$\mathrm{N/A^2}$	$4\pi \cdot 10^{-7}$
Horizontal Mover Mass	M_h	Kg	1.594
Vertical Mover Mass	M_v	Kg	4.350

operated at a sampling frequency of 5 KHz. Control of the magnetic levitation hardware through the interface is implemented using the Quanser Consulting WINCON real-time environment. The software is fully integrated into MATLAB and allows construction of controllers using Simulink diagrams.

The model of the 2DOF testbed is presented next. Let g denote the gravitational acceleration constant, let M_h denote the mass of the platform plus all linear guides, and let M_v denote the mass of the platform plus the pair of vertical guides. Thus, M_h and M_v are the masses of the components that move horizontally and vertically, respectively. Denoting $(x_1, x_2, x_3, x_4) = (y, \dot{y}, x, \dot{x})$ and $(u_1, u_2) = (i_d, i_q)$ and using the expression for the longitudinal and normal forces in (1), (2), we obtain the 2DOF model

$$\begin{bmatrix} \dot{x}_1 \\ \dot{x}_2 \\ \dot{x}_3 \\ \dot{x}_4 \end{bmatrix} = \begin{bmatrix} x_2 \\ g - \frac{K_2(x_1)}{M_v} - \frac{K_3(x_1)}{M_v} u_2 - \frac{K_4(x_1)}{M_v}(u_1^2 + u_2^2) \\ x_3 \\ -\frac{K_1(x_1)}{M_h} u_1 \end{bmatrix}, \tag{3}$$

$$y = \begin{bmatrix} x_1 \\ x_3 \end{bmatrix}. \tag{4}$$

It is clear from (3), (4) that the longitudinal and normal dynamics are coupled. In practice, it is desirable that the longitudinal and normal motions be decoupled. Decoupling is achieved by

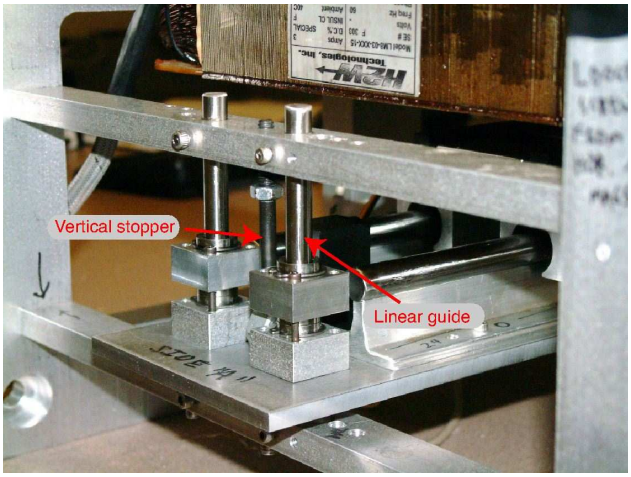

Figure 5: Closeup of vertical linear guides. The linear guides secure the platform and allow for vertical motion. Vertical stoppers are used to prevent the mover from hitting the stator as well as to constrain the vertical motion of the platen during model verification.

control design, as shown below.
In preparation for model validation, let

$$L_1(x_1) = \frac{K_1(x_1)}{M_h}, \; L_i(x_1) = \frac{K_i(x_1)}{M_v}, \quad i = 2, 3, 4,$$

and rewrite $L_i(x_1)$, $i = 1, \ldots, 4$, as

$$L_1(x_1) = C_1 \frac{\tilde{\lambda}(x_1)}{K_c(x_1) \sinh(\frac{\pi}{\tau}(h_m + x_1))}, \tag{5}$$

$$L_2(x_1) = C_2 \tilde{\lambda}(x_1) B_{pmy1}(x_1)^2, \tag{6}$$

$$L_3(x_1) = C_3 \frac{\tilde{\lambda}(x_1) B_{pmy1}(x_1) \coth(\frac{\pi}{\tau}(h_m + x_1))}{K_c(x_1)}, \tag{7}$$

$$L_4(x_1) = C_4 \frac{\tilde{\lambda}(x_1) \coth^2(\frac{\pi}{\tau}(h_m + x_1))}{K_c^2(x_1)}, \tag{8}$$

where $C_1, \ldots, C_4$ are given by

$$C_1 = \frac{12\sqrt{2} W k_{w1} p_m L_A \sigma_m \mu_0 \sinh(\frac{\pi}{\tau} h_m) \sin(\frac{\pi \tau_p}{2\tau})}{M_h \pi p}, \quad C_2 = \frac{L_A p_m \tau}{M_v 4 \mu_0},$$
$$C_3 = -\frac{3\sqrt{2} L_A p_m W k_{w1}}{M_v p^2}, \qquad C_4 = \frac{18 L_A p_m W^2 k_{w1}^2 \mu_0}{M_v \tau p^2}.$$

As noted above, the parameter σ_m in the expressions for $C_1, \ldots, C_4$ is unknown. Also, due to variations in the manufacturing of components, only approximate values of the parameters M_v, M_h, and W in the expressions for $C_1, \ldots, C_4$ are available. In the next section we estimate $C_1, \ldots, C_4$ using a parameter estimation technique.

5 Model Verification Procedure

The model in (3) does not include friction, cogging forces, or end effects. Our goal is thus to verify to what extent these unmodeled effects can be neglected within a reasonable range of operation. A key ingredient in our verification is the noise-perturbed full-state information (NPFSI) estimator of [10], which can be used to estimate parameters (such as $C_1, \ldots, C_4$) that enter linearly in a state equation. See the sidebar "NPFSI estimator" for more details. The NPFSI estimator is used in three different ways, namely, to verify the horizontal dynamics when the vertical motion is constrained; to estimate C_2, C_3, and C_4 and verify the vertical dynamics when the horizontal motion is constrained; and to simultaneously estimate $C_1, \ldots, C_4$ and verify horizontal and vertical dynamics.

We briefly discuss the implementation of the NPFSI estimator. Suppose it is desired to estimate $C_1, \ldots, C_4$ in (3). Two PID regulators are used to determine the inputs u_1 and u_2 to make the horizontal and vertical dynamics approximately track reference signals consisting of a sum of sinusoids at various frequencies. The frequency content of the reference signal must be sufficiently rich for the estimator to converge. The signals $x_1(t), x_3(t), u_1(t), u_2(t)$ generated by the closed-loop system are recorded. Using high-gain observers, the signals $x_2(t) = \dot{x}_1(t)$ and $x_4(t) = \dot{x}_3(t)$ are estimated. The input and estimated state signals are then used by the NPFSI estimator to estimate $C_1, \ldots, C_4$.

Sidebar: "NPFSI Estimator"

The NPFSI estimator of [10] provides a technique for estimating an unknown vector of parameters θ in a nonlinear system of the form

$$\dot{x} = A(x,u)\theta + b(x,u) + \omega(t),$$

where $\omega(t)$ is a bounded disturbance. The estimator relies on a noisy measurement

$$y = x + \nu(t),$$

where $\nu(t)$ is the measurement disturbance. The confidence level in the state measurement is characterized by a positive scalar ε that can be thought of as a bound on the L_2 norm of $\nu(t)$. The estimator is given by

$$\dot{\hat{\theta}} = \varepsilon^{-1}\Sigma^{-1}A(y,u)^T(y-\hat{x}),$$

where

$$\begin{aligned}\dot{\hat{x}} &= A(y,u)\hat{\theta} + b(y,u) + \varepsilon^{-1}(y-\hat{x}),\\ \dot{\Sigma} &= (1-\gamma^{-2})A^T(y,u)A(y,u).\end{aligned}$$

Here, γ is a positive scalar that can be tuned by the user to guarantee estimator convergence. Under suitable assumptions, it is proven in [10] that $\hat{\theta}(t)$ converges to θ as long as a persistency of excitation condition is satisfied and γ is chosen sufficiently large.

5.1 Verification of Horizontal Dynamics

By constraining the air gap to be a constant value $\bar{x}_1$ and setting $u_2 = 0$, the model (3) reduces to

$$\begin{bmatrix} \dot{x}_3 \\ \dot{x}_4 \end{bmatrix} = \begin{bmatrix} x_4 \\ -L_1(\bar{x}_1)u_1 \end{bmatrix}. \tag{9}$$

Applying a constant control input $\bar{u}_1$ and initializing the system with horizontal speed $x_4(0) = 0$, the horizontal displacement $x_3(t)$ of the mover is given by

$$x_3(t) = -\frac{1}{2}L_1(\bar{x}_1)u_1t^2 + x_3(0). \tag{10}$$

This fact is used as follows. For each value $\bar{x}_1^i$ in a predefined set $\{\bar{x}_1^1, \ldots, \bar{x}_1^k\}$, the air gap is constrained by hardware to be at $\bar{x}_1^i$. The mover is started at $x_3(0) = -50$ mm with zero speed. A step input $u_1 = -0.5 \cdot \mathbf{1}(t)$, where $\mathbf{1}(t)$ denotes the unit step function, is imparted to the system, and the resulting horizontal position data are collected. A parabola is fit to the data and an estimate of $L_1(\bar{x}_1^i)$ is obtained by means of (10). For verification, $L_1(\bar{x}_1^i)$ is also approximated by applying the NPFSI estimator to (9).

Experimental results show that the horizontal motion is indeed parabolic, suggesting the correctness of (9). Furthermore, the average error between the estimates of $L_1(\bar{x}_1^i)$ produced by the NPFSI estimator and those arising from curve-fitting parabolas is 3.8%, while the maximum error is 10%. This result reflects the accuracy of the model of the horizontal dynamics and gives confidence in the effectiveness of the NPFSI estimation technique, which is the key verification tool used below.

5.2 Verification of the Vertical Dynamics

By constraining the mover at $x_3 = 0$ mm and setting $u_1 = 0$, the model (3) reduces to

$$\begin{bmatrix} \dot{x}_1 \\ \dot{x}_2 \end{bmatrix} = \begin{bmatrix} x_2 \\ g - L_2(x_1) - L_3(x_1)u_2 - L_4(x_1)u_2^2 \end{bmatrix}. \tag{11}$$

According to the model (11), the current $\bar{u}_2$ needed to maintain the air gap at a desired equilibrium $\bar{x}_1$ satisfies

$$g - L_2(\bar{x}_1) - L_3(\bar{x}_1)u_2 - L_4(\bar{x}_1)u_2^2 = 0.$$

This equation has two roots, one positive and one negative. Since only the negative root is compatible with the physical setup, we set

$$\bar{u}_2 = \frac{-L_3(\bar{x}_1) - \sqrt{L_3^2(\bar{x}_1) - 4L_4(\bar{x}_1)(L_2(\bar{x}_1) - g)}}{2L_4(\bar{x}_1)}. \tag{12}$$

By applying the NPFSI estimator to (11), we obtain estimates of C_2, C_3, and C_4. These estimates are used to determine expressions for the equilibrium currents by replacing (5)–(12). These expressions are evaluated for constant air gaps ranging between 10 and 25 mm with 1 mm increments. The results are compared to experimentally measured equilibrium currents for the same set of air gaps.

The results, shown in Figure 6, indicate that, for air gaps between 15 and 25 mm, the equilibrium currents predicted by the model (11) differ from the experimental values by less than 5%. On the other hand, theoretical and experimental currents diverge for air gaps below 15 mm. The discrepancy for smaller air gaps is the result of physical uncertainties that are not taken into

account within the model. Specifically, experimental evidence in [13] suggests that the cogging force accounts for the bulk of the uncertainty. The cogging force of a linear synchronous motor is the normal force produced by the interaction between the teeth of the stator and the edges of the permanent magnets of the mover. This force is a periodic function of the horizontal position of the mover over the slot pitch of the stator [14].

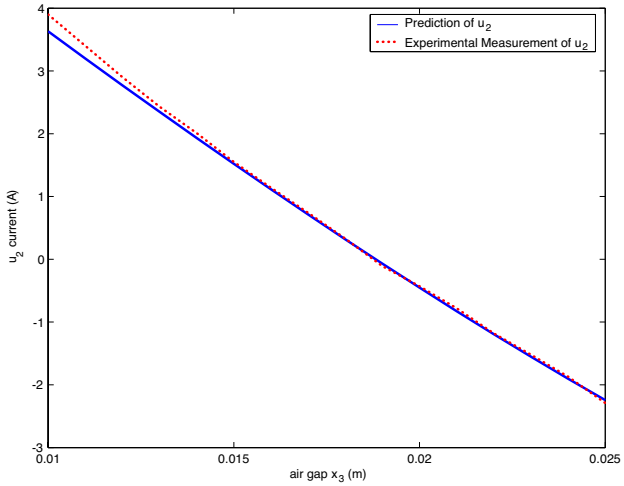

Figure 6: Comparing measured equilibrium currents $\bar{u}_2$ and theoretical predictions. The model of the horizontal dynamics (11), derived from (3), closely predicts the measured current over a wide air gap range, and is less accurate for air gaps smaller than 15 mm. The latter discrepancy between measured equilibrium currents and model predictions is due to the cogging force, which is not accounted for in the model.

5.3 Verification of Complete Model Dynamics

With the horizontal and vertical dynamics of the magnetic levitation model verified separately, we use the NPFSI estimator to simultaneously estimate $C_1, \ldots, C_4$. We substitute the estimated values

$$C_1 = 14.20,\ C_2 = 796.99,\ C_3 = 31.04,\ C_4 = 0.07$$

into (5)–(8) and simulate the model (3), (4). Both the model and experiment are controlled by PID regulators with the same reference signals used to estimate $C_1, \ldots, C_4$. Comparison of the simulated output with the measured output in Figure 7 reflects the accuracy of the model (3).

6 Nonlinear Controller Design and Implementation

It is desirable to design a controller that, besides achieving stabilization or tracking, decouples the longitudinal and normal dynamics. To this end, we use feedback linearization. Define the feedback transformation

$$u_1 = -\frac{v_1}{L_1(x_1)}, \tag{13}$$

$$u_2 = \frac{L_3(x_1) + \sqrt{R(x_1, v_1, v_2)}}{2L_4(x_1)}, \tag{14}$$

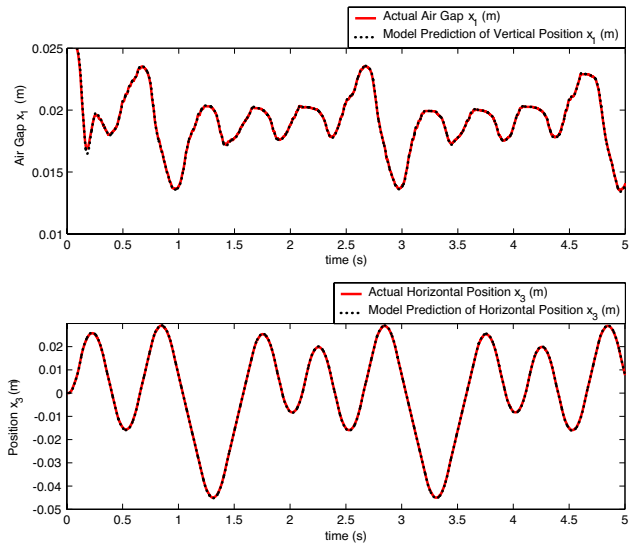

Figure 7: Comparison of the model output over time and the measured output. The parameters $C_1, \ldots, C_4$ in (5)–(8) are determined using the NPFSI estimator. Both the model and the experiment are controlled by PID regulators with the same reference signals used to estimate $C_1, \ldots, C_4$.

where

$$R(x_1, v_1, v_2) = L_3(x_1)^2 + 4L_4(x_1)\left(-v_2 - L_4(x_1)U(x_1, v_1) - L_2(x_1) + g\right), \tag{15}$$

$$U(x_1, v_1) = \left(\frac{v_1}{L_1(x_1)}\right)^2. \tag{16}$$

Replacing (13), (14), (15), and (16) into (3) yields

$$\begin{bmatrix} \dot{x}_1 \\ \dot{x}_2 \\ \dot{x}_3 \\ \dot{x}_4 \end{bmatrix} = \begin{bmatrix} 0 & 1 & 0 & 0 \\ 0 & 0 & 0 & 0 \\ 0 & 0 & 0 & 1 \\ 0 & 0 & 0 & 0 \end{bmatrix} \begin{bmatrix} x_1 \\ x_2 \\ x_3 \\ x_4 \end{bmatrix} + \begin{bmatrix} 0 & 0 \\ 0 & 1 \\ 0 & 0 \\ 1 & 0 \end{bmatrix} \begin{bmatrix} v_1 \\ v_2 \end{bmatrix}, \tag{17}$$

$$y = \begin{bmatrix} x_1 & x_3 \end{bmatrix}^T. \tag{18}$$

Before proceeding further with the design of v_1 and v_2, we note that the feedback transformation (13) and (14) requires that (x, v) belong to the set

$$\mathcal{A} = \{(x, v) : R(x_1, v_1, v_2) \geq 0, L_1(x_1) \neq 0, L_4(x_1) \neq 0\}.$$

Thus, after choosing v_1 and v_2, we need to estimate the range of operation of the device, or the largest set of feasible initial conditions $x(0)$ guaranteeing that $(x(t), v(t)) \in \mathcal{A}$ for all $t \geq 0$. This estimation is performed by Procedure 2 in [9] for a specific choice of v_1 and v_2. Rather than adapting Procedure 2 of [9] to the choice of v below, we verify experimentally that the feedback linearization controller can operate over the range of interest.

We choose v_1 and v_2 to make x_1 and x_3 track a step or a sinusoid of frequency ω_0 or a combination of these. This control specification can be posed as a linear output regulation problem [15], [16],

[17], where the exosystem is

$$\begin{bmatrix} \dot{w}_1 \\ \dot{w}_2 \\ \dot{w}_3 \\ \dot{w}_4 \\ \dot{w}_5 \\ \dot{w}_6 \end{bmatrix} = \begin{bmatrix} 0 & \omega_0 & 0 & 0 & 0 & 0 \\ -\omega_0 & 0 & 0 & 0 & 0 & 0 \\ 0 & 0 & 0 & \omega_0 & 0 & 0 \\ 0 & 0 & -\omega_0 & 0 & 0 & 0 \\ 0 & 0 & 0 & 0 & 0 & 0 \\ 0 & 0 & 0 & 0 & 0 & 0 \end{bmatrix} \begin{bmatrix} w_1 \\ w_2 \\ w_3 \\ w_4 \\ w_5 \\ w_5 \end{bmatrix}, \tag{19}$$

$$\begin{aligned} r_v &= w_1 + w_5, \\ r_h &= w_3 + w_6, \end{aligned} \tag{20}$$

and the output to be regulated is $e = (e_1, e_2) = (x_1 - r_v, x_3 - r_h)$. The internal model has the form

$$\dot{\xi}_v = \phi\xi_v + Ne_1, \quad y_2 = \Gamma\xi_v, \tag{21}$$

$$\dot{\xi}_h = \phi\xi_h + Ne_2, \quad y_1 = \Gamma\xi_h, \tag{22}$$

where

$$\phi = \begin{bmatrix} 0 & 1 & 0 \\ 0 & 0 & 1 \\ 0 & -\omega_0^2 & 0 \end{bmatrix}, \quad N = \begin{bmatrix} 0 \\ 0 \\ 1 \end{bmatrix}, \quad \Gamma = [1\ 0\ 0].$$

The subsystems (21) and (22) are internal models for the vertical and horizontal dynamics, respectively. Since the tracking errors e_1 and e_2 are available for feedback and $\dot{e}_1$, $\dot{e}_2$ can be estimated using high-gain observers, we complete the output regulator design by letting

$$v_1 = K_h \begin{bmatrix} e_2 & \dot{e}_2 & \Gamma\xi_h \end{bmatrix}^{\mathrm{T}}, \tag{23}$$

$$v_2 = K_v \begin{bmatrix} e_1 & \dot{e}_1 & \Gamma\xi_v \end{bmatrix}^{\mathrm{T}}, \tag{24}$$

where K_h and K_v are chosen to stabilize the augmented system

$$\begin{bmatrix} \dot{x}_1 \\ \dot{x}_2 \\ \dot{x}_3 \\ \dot{x}_4 \\ \dot{\xi}_v \\ \dot{\xi}_h \end{bmatrix} = \begin{bmatrix} x_2 \\ v_2 + \Gamma\xi_v \\ x_4, \\ v_1 + \Gamma\xi_h \\ \phi\xi_v + Nx_1 \\ \phi\xi_h + Nx_3 \end{bmatrix}. \tag{25}$$

The final controller is thus given by (13), (14), (21), (22), (23), and (24). The controller block diagram is depicted in Figure 8.

7 Experimental Results

The nonlinear controller is implemented using WINCON. The ability of the controller to track step and sinusoidal signals is evaluated and compared with linear controllers.

7.1 Setpoint Tracking Performance of the Nonlinear Controller

The gains K_h and K_v in (23) and (24) are chosen by applying pole placement to (25). The poles corresponding to the horizontal dynamics, chosen by trial and error tuning, are placed at

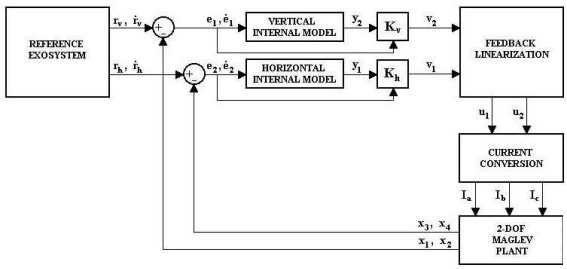

Figure 8: Block diagram of nonlinear controller. The tracking errors are fed to two internal models. Following the internal model principle, a state feedback controller stabilizes the cascade of plant and internal models when $r_v \equiv r_h \equiv 0$. The resulting control input (v_1, v_2) is then used to generate $(u_1, u_2) = (i_q, i_d)$ by means of a feedback transformation. Finally, the pair (i_q, i_d) is converted to three-phase currents, which are fed to the LCAMs to control the maglev apparatus.

$[-9, -10, -11, -12, -13]$, while the poles corresponding to the vertical dynamics are placed at $[-11, -12, -13, -14, -15]$. This choice gives

$$K_h = \begin{bmatrix} -1182 & -55 & -154440 & -45128 & -11924 \end{bmatrix},$$
$$K_v = \begin{bmatrix} -1662 & -65 & -360360 & -103350 & -20332 \end{bmatrix}.$$

The resulting nonlinear controller is used to make the system stabilize five consecutive setpoints over the ranges $[-50 \text{ mm}, 50 \text{ mm}]$ horizontal and $[15 \text{ mm}, 25 \text{ mm}]$ vertical. Figure 9 shows the response of the vertical system states $x_1(t)$ and $x_2(t)$ to the step commands, and the absolute vertical positioning error. In all cases, the vertical tracking error settles below 0.1 mm in less than 1.3 s. Figure 10 displays the experimental results involving the horizontal system states $x_3(t)$ and $x_4(t)$. For the first four steps the horizontal tracking error settles below 0.1 mm in less than 1.2 s, whereas the fifth step requires 2.38 s. In additional experiments, not shown here, the controller drives the tracking error to within encoder resolution 10 μm in about 10 s.
By tuning the controller gains, it is possible to emphasize certain performance specifications. For instance, to reduce the overshoot in the vertical dynamics at the expense of increasing the settling time, after trial and error tuning we place the poles corresponding to the vertical dynamics at $[-57.9, -9.9 + 11.3\,i, -9.9 - 11.3\,i, -1.6 + 1.4\,i, -1.6 - 1.4\,i]$, obtaining

$$K_v = \begin{bmatrix} -1592 & -81 & -55736 & -11573 & -15825 \end{bmatrix}.$$

Figure 11 shows that the step response now exhibits much smaller vertical overshoot at the expense of a longer time needed for the tracking error to settle below 0.1 mm (still below 3 s). This tradeoff between overshoot and settling time, which is an intrinsic characteristic of the problem, arises from the fact that we are displacing a rigid body using forces of fixed maximum magnitude. Depending on the final industrial application, either the overshoot or settling time may be a more important factor. The results show that controller adjustments can accommodate either requirements.
We next compare the performance of the nonlinear controller with a linearization-based controller in tracking two setpoints. Specifically, we use the linear output regulator in (21)–(24) without using the feedback transformation (13) and (14). To make a fair comparison, the model in (3) is linearized about equilibria corresponding to the desired setpoints. For each linear model, the gains K_h, K_v are chosen so that the poles of the closed-loop system coincide with the poles induced by the nonlinear controller in the feedback-linearized plant. The first step command, shown in Figure 12,

has small amplitude, starting from the initial condition $(0.026\ \text{m}, 0, 0, 0)$ and having final value $(0.024\ \text{m}, 0, 0.005\ \text{m}, 0)$. The second step command is larger, starting at the same initial condition as before but terminating at $(0.018\ \text{m}, 0, 0.020\ \text{m}, 0)$.
The results show that while both the linear and nonlinear controller can handle a small step command, the linear response demonstrates a much larger transient and longer settling time. When subjected to the larger step command, the linear controller destabilizes the plant, while the nonlinear controller continues to exhibit excellent performance. Note that around 5.5 s, the instability exhibited by the linear controller causes a safety mechanism within the real-time code to shut down the system, at which time the oscillations halt; see Figure 12.

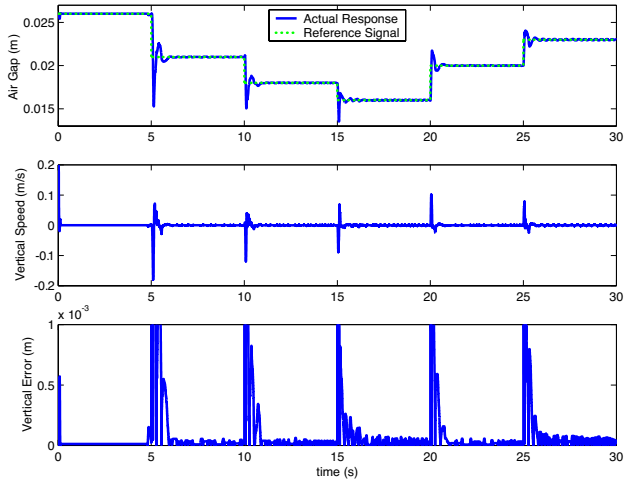

Figure 9: Vertical motion in response to setpoint commands using the nonlinear feedback linearization controller. The vertical positioning error is also included. Setpoint tracking is achieved with the required accuracy of 0.1 mm. While the transient is fast, the large overshoot of 114% at $t = 5$ s is undesirable.

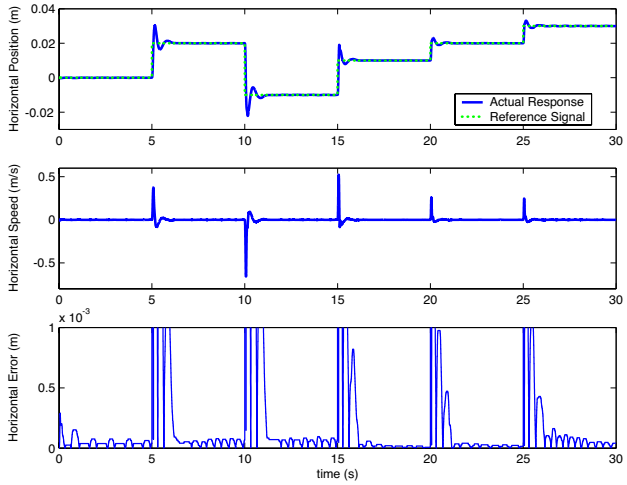

Figure 10: Horizontal motion in response to setpoint commands using the nonlinear feedback linearization controller. The horizontal positioning error is also included. Setpoint tracking is achieved with the required accuracy of 0.1 mm. The maximum overshoot is 43%.

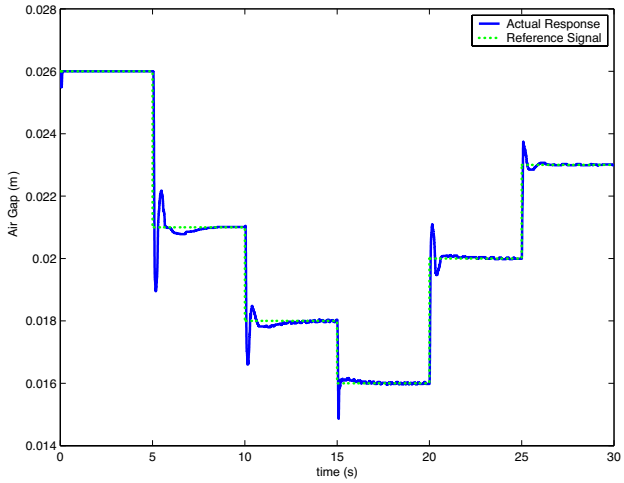

Figure 11: Vertical step response when the nonlinear controller gains are adjusted. The overshoot of 40% at $t = 5$ s is much smaller than that in Figure 9. However, the settling time increases by 200%.

7.2 Sinusoidal Tracking Performance of Nonlinear Controller

For the tracking experiments, we choose $r_h(t)$ and $r_v(t)$ to be sinusoidal signals with amplitudes 30 mm and 5 mm, respectively, and the same frequency $\omega_0 = 1.5\pi$ rad/s. The vertical reference $r_v(t)$ also includes an offset of 20 mm. The same controller gains used for setpoint tracking are employed for sinusoidal tracking. Figure 13 summarizes the tracking results obtained using the nonlinear feedback linearization controller. The average horizontal tracking error is about 0.11 mm, with occasional peaks that reach 0.4 mm. The average vertical tracking error is 0.24 mm, with peaks that reach 0.8 mm. The major factor limiting the tracking performance is the misalignment of the linear guides.

8 A 3DOF Microstepper

Having assessed the accuracy of the mathematical model of the forces developed by one PMLSM and the effectiveness of a nonlinear control strategy to control two DOFs, it remains to be seen whether the approach can be extended to more than two DOFs. The device shown in Figure 14, built by Quanser Consulting, controls three DOFs by means of four PMLSMs combined into two pairs by wiring in parallel the three phases of each pair. The system therefore has four control inputs, namely, direct and quadrature currents for the two pairs of linear motors. The four movers are fixed on a honeycomb aluminum platform that sits on three pairs of orthogonally mounted linear guides. If, instead of being wired in pairs, the PMLSMs were individually controlled, then the microstepper would produce 6DOF motion. In the setup of Figure 14, however, the linear guides constrain the motion to be purely translational. As in the 2DOF setup, this setup allows for easy incorporation of sensors.

The mathematical model of the 3DOF device is a straightforward extension of (3) and is therefore omitted. Extensions of model verification procedures developed in previous sections are used to assess the validity of the mathematical model of the device. The horizontal and vertical operating regions of the device are $[-50\text{ mm}, 50\text{ mm}] \times [-50\text{ mm}, 50\text{ mm}]$ and $[20\text{ mm}, 30\text{ mm}]$, respectively. The controller we use to operate this microstepper is similar to the one in (13), (14), (21), (22),

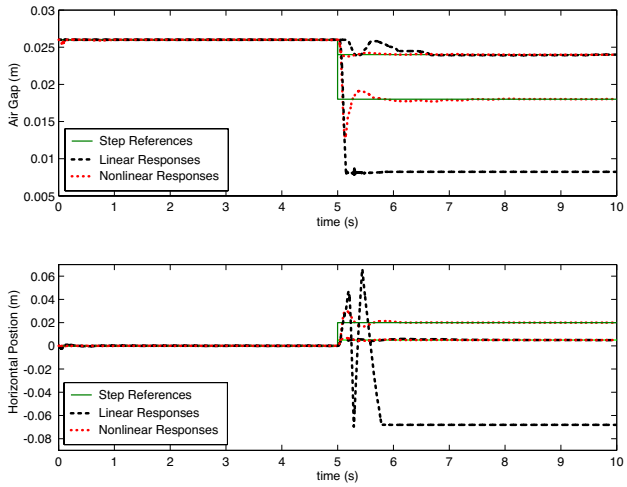

Figure 12: Experimental comparison of two step responses of linear and nonlinear controllers. Both controllers successfully handle a step response of small amplitude, although the linear controller yields poor transient performance. On the other hand, the linear controller destabilizes the plant for a larger step commmand.

(23), and (24) developed for the 2DOF microstepper, but enhanced with an antiwindup mechanism. To demonstrate the controller, we present experimental results for setpoint and sinusoidal tracking. Figure 15 shows the output response of the 3DOF microstepper to five setpoint commands. Figure 16 shows the corresponding tracking errors. In all cases, the position error settles below 0.1 mm in less than 3 s and to the encoder resolution of 10 μm in less than 5 s. Figures 17 and 18 show the output response and tracking error when the microstepper is subjected to a sinusoidal reference command. The average x-axis and z-axis tracking errors are about 0.12 mm and 0.13 mm, respectively. The average y-axis tracking error is 59 μm. These results indicate that the 3DOF microstepper is more precise than the 2DOF microstepper because of better alignment of the linear guides. Recall that the control design produces current references for the linear current amplifiers. The tracking errors in Figure 16 are likely due to transients in the current dynamics.

Conclusions and Future Work

We demonstrated the feasibility of using iron-cored PMLSMs to develop microsteppers with multiple DOFs. To do this, we investigated the accuracy of the mathematical model (1), (2) of the forces generated by one PMLSM as well as the performance of a nonlinear feedback linearization controller. We demonstrated that several PMLSMs together can control three DOFs. In both experimental setups, linear guides are used to constrain the motion to be purely translational. Linear guides entail friction, which is undesirable in the photolithography process. Future research involves eliminating linear guides and controlling six DOFs (translations and rotations of the platform). To control six DOFs without linear guides, more sophisticated sensors are required, and the four PMLSMs in the setup of Figure 14 must be individually controlled.

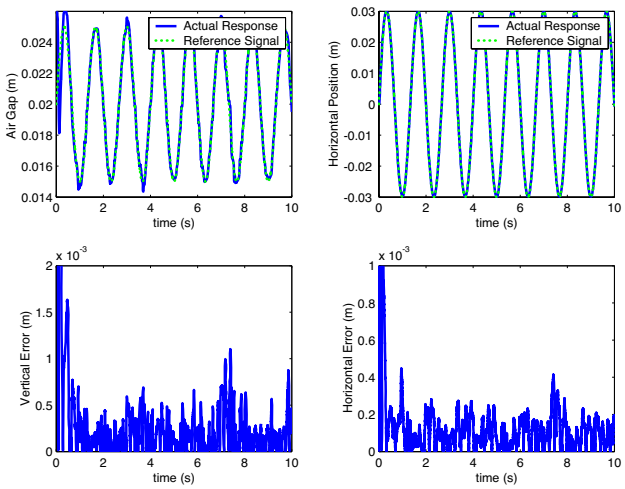

Figure 13: Output response to sinusoidal reference inputs using the nonlinear feedback linearization controller. The references $r_v(t)$ and $r_h(t)$ are chosen so that the platform moves along an ellipsoidal contour across the complete range of operation.

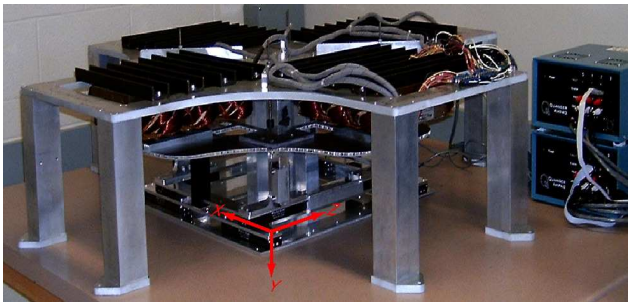

Figure 14: 3DOF magnetic levitation hardware implementation. The heavy aluminum frame supports four PMLSM stators. A honeycomb aluminum platform, placed on top of three pairs of orthogonally mounted linear guides, supports the four movers.

Acknowledgments

This research was supported by the Natural Sciences and Engineering Research Council of Canada (NSERC) and the Canada Foundation for Innovation (CFI). Brydon Owen was partially supported by the Canadian Space Agency (CSA).

References

[1] K.-Y. Tsai and J.-Y. Yen, "Servo system design of a high-resolution piezo-driven fine stage for step-and-repeat microlithography systems," in *The 25th Annual Conference of the IEEE Industrial Electronics Society*, vol. 1, 1999, pp. 11–16.

[2] S. Middleman and A. K. Hochberg, *Process Engineering Analysis in Semiconductor Device Fabrication*. McGraw-Hill, New York, 1993.

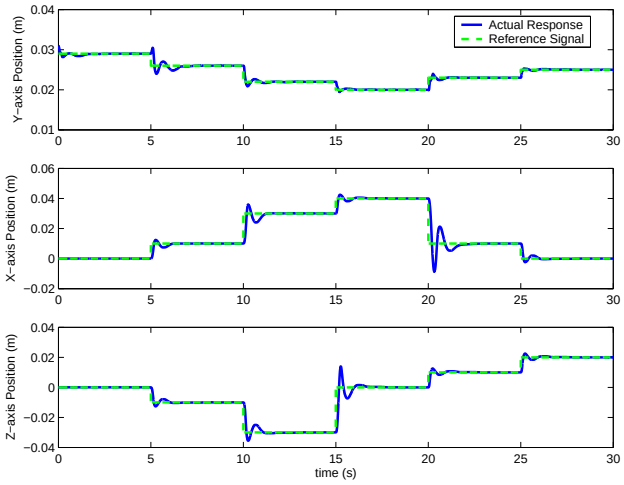

Figure 15: Response of the 3DOF microstepper to setpoint commands. By incorporating anti-windup into the nonlinear controller design from the 2DOF setup, the 3DOF microstepper achieves setpoint tracking to within encoder resolution across the complete operating range of the device.

[3] X. Shan, S.-K. Kuo, J. Zhang, and C.-H. Menq, "Ultra precision motion control of a multiple degree of freedom magnetic suspension stage," *IEEE/ASME Transactions on Mechatronics*, vol. 7, no. 1, pp. 67–78, March 2002.

[4] F. Auer and H. F. van Beek, "Practical application of a magnetic bearing and linear propulsion unit for six degree of freedom positioning," in *Fourth International Symposium on Magnetic Bearings*, Zurich,Switzerland, August 1994, pp. 183–188.

[5] A. Molenaar, F. Auer, and H. F. van Beek, "Application of magnetic bearing for contactless ultra high precision positioning," in *Fifth International Symposium on Magnetic Bearings*, Kanazawa, Japan, August 1996, pp. 441–445.

[6] A. Molenaar, E. H. Zaaijer, and H. F. van Beek, "A novel low dissipation long stroke planar magnetic suspension and propulsion stage," in *Sixth International Symposium on Magnetic Bearings*, Boston, MA, USA, August 1998, pp. 650–659.

[7] W. Kim and D. Trumper, "High-precision levitation stage for photolithography," *Precision Engineering*, vol. 22, pp. 66–67, 1998.

[8] W. Kim, D. L. Trumper, and J. H. Lang, "Modeling and vector control of planar magnetic levitator," *IEEE Transactions on Industry Applications*, vol. 34, no. 6, pp. 1254–1262, November/December 1998.

[9] M. Maggiore and R. Becerril, "Modeling and control design for a magnetic levitation system," *International Journal of Control*, vol. 77, no. 10, pp. 964–977, 2004.

[10] G. Didinsky, Z. Pan, and T. Basar, "Parameter identification for uncertain plants using $\mathcal{H}^\infty$ methods," *Automatica*, vol. 31, no. 9, pp. 1227–1250, 1995.

[11] S. Nasar and G. Xiong, "Determination of the field of a permanent-magnet disk machine using the concept of magnetic charge," *IEEE Transactions on Magnetics*, vol. 24, no. 3, pp. 2038–2044, May 1988.

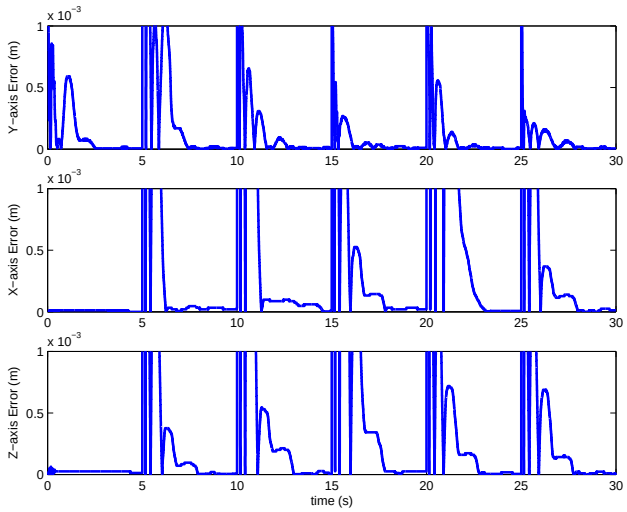

Figure 16: Position error of the 3DOF microstepper in response to sepoint commands. In all cases, the position error settles below 0.1 mm in less than 3 s and to encoder resolution of 10 μm in less than 5 s.

[12] G. Xiong and S. A. Nasar, "Analysis of fields and forces in a permanent magnet linear synchronous machine based on the concept of magnetic charge," *IEEE Transactions on Magnetics*, vol. 25, no. 3, pp. 2713–2719, May 1989.

[13] R. B. Owen and M. Maggiore, "Implementation and model verification of a magnetic levitation system," in *Proc. American Control Conference*, Portland, OR, 2005, pp. 1142–1147.

[14] R. Cruise and C. Landy, "Reduction of cogging forces in linear synchronous motors," in *IEEE Africon 1999*, vol. 2, 1999, pp. 623–626.

[15] E. J. Davison, "The robust control of a servomechanism problem for linear time-invariant multivariable systems," *IEEE Transactions on Automatic Control*, vol. 21, pp. 25–34, 1976.

[16] B. A. Francis and W. M. Wonham, "The internal model principle of control theory," *Automatica*, vol. 12, pp. 457–465, 1976.

[17] B. A. Francis, "The linear multivariable regulator problem," *SIAM Journal on Control and Optimation*, vol. 14, pp. 486–505, 1977.

Robert Brydon Owen graduated from the University of Manitoba in 2003 with a B.S. in electrical engineering, and the University of Toronto in 2005 with a Masters of Applied Science in systems control from the Department of Electrical Engineering. Currently, he is employed at New Flyer Industries as an engineer-in-training. Recently, he was awarded the 2005 IEEE CCA Best Student Paper Award for his work on magnetic levitation. His interests include system identification, model verification, and the application of nonlinear control design and analysis to practical industrial problems.

Manfredi Maggiore received the "Laurea" degree in electronic engineering in 1996 from the University of Genoa, Italy, and the Ph.D. degree in electrical engineering from the Ohio State

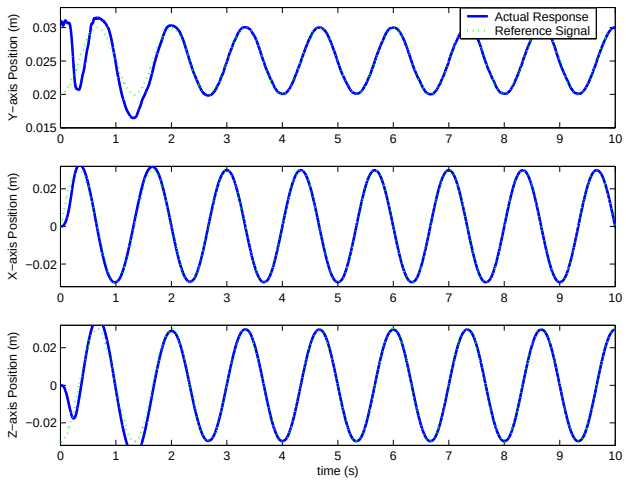

Figure 17: Response of the 3DOF microstepper to a sinusoidal command. By applying simultaneous sinusoidal reference commands across each axis of motion, the 3DOF microstepper tracks a contour over the complete operating range of the microstepper.

University, USA, in 2000. He is currently an assistant professor in the Edward S. Rogers Sr. Department of Electrical and Computer Engineering, University of Toronto, Canada. His research interests are in nonlinear geometric control and magnetic levitation.

Jacob Apkarian received the B.Eng. degree from McGill University in 1980 and the M.A.Sc. and Ph.D. degrees from the University of Toronto in 1984 and 1988, respectively. He was an assistant professor at the University of British Columbia from 1989 to 1990 and a senior controls engineer at SPAR Aerospace (now MDA Robotics) from 1992 to 1996. He founded Quanser Consulting in 1990.

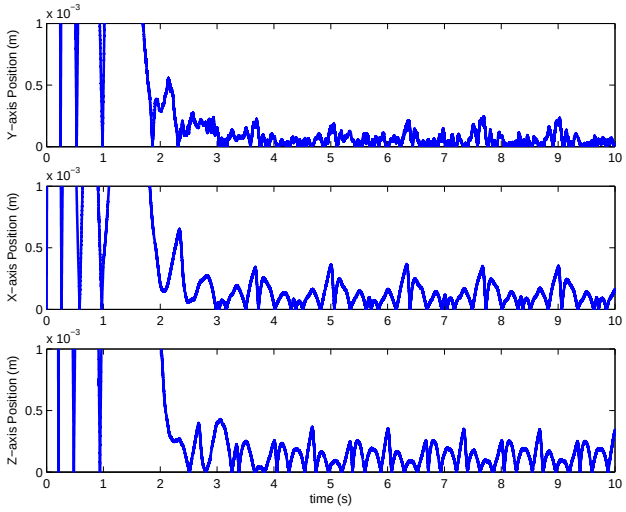

Figure 18: Tracking error of the 3DOF microstepper in response to sinusoidal references. The tracking performance is significantly better than that of the 2DOF microstepper, due to better alignment of the linear guides.